(12)

RADC-TR-84-45
In-House Report
March 1984

AD-A147 367

EFFICIENT COMPUTATION OF REFLECTOR ANTENNA APERTURE DISTRIBUTIONS AND FAR FIELD PATTERNS

Hans Steyskal
Robert A. Shore

APPROVED FOR PUBLIC RELEASE; DISTRIBUTION UNLIMITED

DTIC
ELECTE
NOV 14 1984
S D

ROME AIR DEVELOPMENT CENTER
Air Force Systems Command
Griffiss Air Force Base, NY 13441

DTIC FILE COPY

84 11 05 083

This report has been reviewed by the RADC Public Affairs Office (PA) and is releasable to the National Technical Information Service (NTIS). At NTIS it will be releasable to the general public, including foreign nations.

RADC-TR-84-45 has been reviewed and is approved for publication.

APPROVED:

JOHN K. SCHINDLER
Chief, Antennas & RF Components Branch
Electromagnetic Sciences Division

APPROVED:

ALLAN C. SCHELL
Chief, Electromagnetic Sciences Division

FOR THE COMMANDER:

JOHN A. RITZ
Acting Chief, Plans Office

If your address has changed or if you wish to be removed from the RADC mailing list, or if the addressee is no longer employed by your organization, please notify RADC (EEA) Hanscom AFB MA 01731. This will assist us in maintaining a current mailing list.

Do not return copies of this report unless contractual obligations or notices on a specific document requires that it be returned.

Unclassified

SECURITY CLASSIFICATION OF THIS PAGE (When Data Entered)

REPORT DOCUMENTATION PAGE		READ INSTRUCTIONS BEFORE COMPLETING FORM
1. REPORT NUMBER RADC-TR-84-45	2. GOVT ACCESSION NO. A147367	3. RECIPIENT'S CATALOG NUMBER
4. TITLE (and Subtitle) EFFICIENT COMPUTATION OF REFLECTOR ANTENNA APERTURE DISTRIBUTIONS AND FAR FIELD PATTERNS		5. TYPE OF REPORT & PERIOD COVERED In-house 6. PERFORMING ORG. REPORT NUMBER
7. AUTHOR(s) Hans Steyskal Robert A. Shore		8. CONTRACT OR GRANT NUMBER(s)
9. PERFORMING ORGANIZATION NAME AND ADDRESS Rome Air Development Center (EEA) Hanscom AFB Massachusetts 01731		10. PROGRAM ELEMENT, PROJECT, TASK AREA & WORK UNIT NUMBERS PE 62702F 2305J303
11. CONTROLLING OFFICE NAME AND ADDRESS Rome Air Development Center (EEA) Hanscom AFB Massachusetts 01731		12. REPORT DATE March 1984 13. NUMBER OF PAGES 47
14. MONITORING AGENCY NAME & ADDRESS(if different from Controlling Office)		15. SECURITY CLASS. (of this report) Unclassified 15a. DECLASSIFICATION/DOWNGRADING SCHEDULE N/A

16. DISTRIBUTION STATEMENT (of this Report)

Approved for public release; distribution unlimited.

17. DISTRIBUTION STATEMENT (of the abstract entered in Block 20, if different from Report)

18. SUPPLEMENTARY NOTES

RADC Project Engineer: Hans Steyskal, RADC/EEA

19. KEY WORDS (Continue on reverse side if necessary and identify by block number)

Reflector antenna
Pattern analysis
Beam scanning
Limited scan
Array-fed reflector

20. ABSTRACT (Continue on reverse side if necessary and identify by block number)

A computationally efficient method is presented for calculating the aperture distribution and the far field pattern of a parabolic reflector with an off-axis array feed. Idealized, uncoupled array elements and realistic, mutually coupled, circular waveguide elements are considered. Ray optics are used to determine the scalar aperture field over a rectangular grid of aperture sampling points. Two alternative methods for performing the aperture integration required for the pattern evaluation are compared: (a) based on summation of subapertures with constant amplitude/linear phase, and (b) based on the Fast

DD FORM 1 JAN 73 1473

Unclassified

SECURITY CLASSIFICATION OF THIS PAGE (When Data Entered)

20. Abstract - Contd.

Fourier Transform (FFT) and sampling theory. Patterns obtained with this method are compared with independently computed patterns that use other approaches. The range of validity of the aperture field integration method is discussed.

Accession For
NTIS GRA&I ☒
DTIC TAB ☐
Unannounced ☐
Justification
By
Distribution/
Availability Codes
Dist | Avail and/or Special
A-1

Contents

1. INTRODUCTION 5

2. THEORY 6

2.1 Aperture Distribution 6
2.2 Far Field Pattern 10

3. APERTURE BLOCKAGE 12

4. ILLUSTRATIVE EXAMPLES OF COMPUTED PATTERNS 13

5. CONCLUSIONS 22

REFERENCES 23

APPENDIX A: FEED ARRAY PATTERN 25

APPENDIX B: FEED-APERTURE MAPPING 33

APPENDIX C: VALIDITY OF THE APERTURE INTEGRATION METHOD 41

Illustrations

1. Parabolic Reflector With Feed Array 7
2. Ray Path From Feed to Reflector to Aperture 9
3. Blockage Limited Sidelobe Level L_{block} vs Feed/Reflector Diameter Ratio d/D 13
4. Pattern Computed for a Uniform Aperture D=200λ With $\tau = 4\lambda$ 14
5. Pattern Computed for a Uniform Aperture With Aperture Sample Spacing Increased From $\tau=4\lambda$ to $\tau=8\lambda$ 16
6. Pattern Computed for a Uniform Aperture With Aperture Sample Spacing Increased to $\tau=12\lambda$ 16

7a. Pattern in the u-plane Through the Main Beam at $u_o=0.05$, $v_o=0$ 19

7b. Pattern in the v-plane Through the Main Beam at $u_o=0.05$, $v_o=0$ 19

A1. Feed Coordinate System 26

A2. Waveguide Element With Aperture Matching Section 29

B1. Ray Trajectory From Feed to Aperture 34

C1. Comparison of Patterns Obtained by Scalar Aperture Field Integration (Solid Line) and by Vector Current Integration (Circles) 42

C2. Geometry of Parabolic Reflector With Line Source Feed 43

C3. Reflector Edge Geometry for GTD Analysis 45

Tables

1. Sidelobe Positions and Amplitudes - Comparison of Scalar and Vector Field Approaches 15
2. Sidelobe Positions and Amplitudes - Dependence on Aperture Sample Spacing τ 18

3a. Sidelobe Positions and Amplitudes in u-plane Cut Through Main Beam - Comparison of Scalar and Vector Field Approaches 20

3b. Sidelobe Positions and Amplitudes in v-plane Cut Through Main Beam - Comparison of Scalar and Vector Field Approaches 21

4. Computer Time for One Pattern Cut Over 20 Beamwidths 22

Efficient Computation of Reflector Antenna Aperture Distributions and Far Field Patterns

1. INTRODUCTION

The classic subject of reflector antennas has received considerable interest in the last few years. The reason is that an antenna system composed of a reflector and a feed-array combines two very attractive features, namely the inexpensive high gain of a reflector and the flexibility of an array for beam shaping or scanning. A recent effort at the RADC/Electromagnetic Sciences Division has been directed at developing computational capabilities for such antenna systems and studying a limited scan technique using a paraboloidal reflector with a small planar array feed.

A basic component of such an antenna study is a computational method to obtain the far field pattern corresponding to the particular antenna configuration of interest. Since there are many design parameters including the feed-array location and orientation, the array lattice, and the element number and excitation, this method must be computationally efficient in order to avoid prohibitive computer costs. But, the relative merits of a particular design can usually be judged from a limited pattern sector, covering the main beam and close-in sidelobes of the copolarized antenna pattern. This suggests an approach based on aperture integration, which is highly accurate for the main beam region; and on the use of scalar theory, which is a significant computational simplification.

(Received for publication 20 March 1984)

The subject of this report is the presentation of this computation method. We believe the method to have two novel features, not previously reported in the vast literature on reflector antennas. These are the use of analytic expressions based on geometrical optics to map the radiation from the off-axis feed onto the reflector aperture, and the use of a rectangular grid of aperture sampling points, which simplifies the pattern computation. An attractive feature of this approach is that in the process we determine the aperture distribution, which often is of diagnostic value. Two different methods of aperture integration are pursued, one based on summation of subapertures with constant amplitude/linear phase excitation and the other based on the Fast Fourier Transform (FFT) and sampling theory.[1]

2. THEORY

2.1 Aperture Distribution

Consider a rotationally symmetric parabolic reflector fed by a small, planar array with arbitrary location and orientation, as shown in Figure 1. The reflector vertex is located at the origin of the x, y, z -coordinate system and the reflector axis coincides with the z-axis. The direction to the observation point is (θ, ϕ), where θ and ϕ are standard spherical coordinates. The reflector surface is given by the equation,

$$4\,Fz = x^2 + y^2, \quad z \le D^2/16F \quad , \tag{1}$$

where F is the focal length and D is the diameter of the reflector.

The feed array has its own local x'y'z'-coordinate system, whose origin is located at (x_f, y_f, z_f) and whose z'-axis forms the angle θ_z with the positive z-axis.

We treat the antenna in the transmit mode and apply to the feed the input power P_i, which is divided into radiated power P_{rad} and reflected power P_{ref}. From the feed we trace a ray tube of solid angle cross-section $d\Omega$ through its reflection point on to the aperture, where it intercepts an area dA. Thus, the complex aperture distribution is given by

1. Bucci, O.M., Franceschetti, G., and D'Elia, G. (1980) Fast analysis of large antennas - A new computational philosophy, IEEE Trans. Antennas Propag. 28:306.

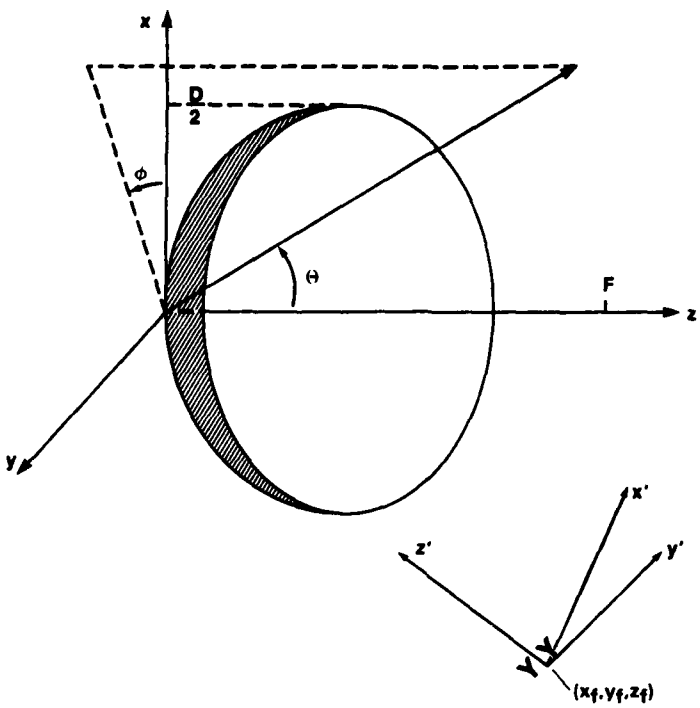

Figure 1. Parabolic Reflector With Feed Array

$$\rho = \left[\frac{P_{rad}}{4\pi} \frac{d\Omega}{dA} \right]^{1/2} f(\Omega)\, e^{-jk(s_f + s_a)} \quad , \tag{2}$$

where the complex feed pattern $f(\Omega)$ is normalized such that $|f(\Omega)|^2$ represents the directivity in the direction Ω, k denotes the wavenumber, and s_f and s_a are the distances along the ray from the feed to the reflector and from the reflector to the aperture, respectively. Note that ρ is a "field quantity" and the intensity $|\rho|^2$ has the dimension of power per unit area.

The antenna pattern is easily obtained in terms of the aperture distribution. The aperture directivity in the observation direction (θ, ϕ) is

$$G_{ap}(\theta,\phi) = \frac{4\pi}{\lambda^2} \frac{\left| \int \rho\, e^{jk\bar{u} \cdot \bar{r}_a}\, dA \right|^2}{\int |\rho|^2\, dA}$$

$$= \frac{4\pi}{\lambda^2} \frac{\left| \iint \rho\, e^{jk(x_a \cos\phi + y_a \sin\phi)\cos\theta}\, dx_a\, dy_a \right|^2}{\iint |\rho|^2\, dx_a\, dy_a} \quad , \tag{3}$$

where $\mathbf{u} = (u, v, w) = (\sin\theta\cos\phi,\ \sin\theta\sin\phi,\ \cos\theta)$ is the unit vector in the direction of observation and $r_a = (x_a, y_a, z_a)$ is the position vector of the aperture element dA. The gain pattern of the antenna system, which includes spillover losses but neglects reflected feed power, is

$$G_o = G_{ap} \frac{\int |\rho|^2 \, dA}{P_{rad}} \quad . \tag{4}$$

Similarly, the total gain, including spillover and reflected feed power is

$$G_t = G_{ap} \frac{\int |\rho|^2 \, dA}{P_i} \quad . \tag{5}$$

Equations (2) and (3) form the basis for the computer evaluation of the aperture distribution ρ and the antenna pattern G_{ap}.

Returning to Eq. (2) we note that the feed characteristics are described entirely by the feed far-field pattern $f(\Omega)$. This requires that all points on the reflector indeed be in the far field of the feed array. However, it turns out that this condition is not overly restrictive. For example, a 100λ reflector diameter and 50λ focal length allows up to 5λ feed diameters.

In order to obtain a correct value for the absolute gain G_o it is essential that the feed pattern $f(\Omega)$ be very accurately known. The main difficulty lies in determining the total radiated power P_{rad}, which involves integrating the feed pattern over 4π steradians. In Appendix A we derive the feed pattern corresponding to two different feed-array elements: idealized $\cos\theta$-elements, and realistic circular waveguide elements.

The remaining quantities in Eq. (2), the mapping function $d\Omega/dA$ and ray path lengths s_f and s_a, are purely geometric quantities, which depend solely on the coordinates (x_f, y_f, z_f) of the feed center P_f and the coordinates (x_a, y_a, z_a) of the aperture point P_a (see Figure 2). Unfortunately, they are nonlinear functions of these coordinates and in order to derive explicit expressions for them we must first determine the coordinates (x_r, y_r, z_r) of the ray reflection point P on the paraboloid. We use the fact that the ray path P_f-P_r-P_a obeys Fermat's principle and determine P_r by numerical minimization. Thus, we let the computer search for the minimum of the total path length

$$s = s_f + s_a = \text{minimum} \quad , \tag{6}$$

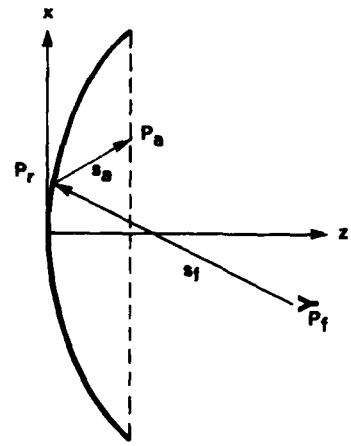

Figure 2. Ray Path From Feed to Reflector to Aperture

where

$$s_f = [(x_f - x_r)^2 + (y_f - y_r)^2 + (z_f - z_r)^2]^{1/2}$$

$$s_a = [(x_r - x_a)^2 + (y_r - y_a)^2 + (z_r - z_a)^2]^{1/2}$$

$$z_r = (x_r^2 + y_r^2)/4F$$

$$z_a = D^2/16F \quad . \tag{7}$$

This proved to be a simple and efficient approach since fast minimization subroutines for the computer are readily available. The actual derivation of the analytic expression for the mapping $d\Omega/dA$ is discussed in Appendix B. This concludes the derivation of the complex aperture distribution.

2.2 Far Field Pattern

We determine the far field pattern G_a by numerical integration of Eq. (3). For this purpose we approximate the circular aperture distribution by a sum of square subapertures with constant amplitude and linear phase distribution. This clearly results in a rather jagged reflector rim, but since we are interested in

an area integral this is of no consequence, as long as we make the division into squares fine enough so as to adequately approximate the aperture area. In most cases this represents a rather mild bound on the square size τ. A more restrictive bound originates from the aperture distribution approximation. This requires τ to be small enough so that across each subaperture the distribution can be approximated as

$$\rho(x_a, y_a) \simeq \rho(x_{an}, y_{an})\, e^{j[\psi_{xn}(x_a - x_{an}) + \psi_{yn}(y_a - y_{an})]} \quad , \tag{8}$$

where (x_{an}, y_{an}) denotes the center of the n:th subaperture, and the x- and y-components of the phase gradient at this point are ψ_{xn} and ψ_{yn}. These components are taken as the average phase slope between the centers of the two subapertures on either side of subaperture n, which leads to

$$\psi_{xn} = [\arg \rho(x_{an} + \tau, y_{an}) - \arg \rho(x_{an} - \tau, y_{an})]/2\tau$$

$$\psi_{yn} = [\arg \rho(x_{an}, y_{an} + \tau) - \arg \rho(x_{an}, y_{an} - \tau)]/2\tau \quad . \tag{9}$$

At the reflector edge, where these expressions do not apply, we average only over the distance τ between the centers of the subaperture at the edge and its interior neighbor. With the approximation (8) the integrals appearing in Eq. (3) now reduce to

$$\int_{\text{aperture}} \rho\, e^{jk\bar{u}\cdot\bar{r}_a}\, dA$$

$$\simeq \sum_n \iint_{\text{subaperture } n} \rho(x_{an}, y_{an})\, e^{j[\psi_{xn}(x_a - x_{an}) + \psi_{yn}(y_a - y_{an})]}\, e^{jk(ux_a + vy_a)}\, dx_a\, dy_a$$

$$= \tau^2 \sum_n \rho(x_{an}, y_{an})\, \text{sinc}\, \frac{\tau(ku + \psi_{xn})}{2}\, \text{sinc}\, \frac{\tau(kv + \psi_{yn})}{2}\, e^{ik(ux_{an} + vy_{an})} \tag{10}$$

and

$$\int_{\text{aperture}} |\rho|^2\, dA \simeq \tau^2 \sum_n |\rho(x_{an}, y_{an})|^2 \quad . \tag{11}$$

This completes the derivation of the far field pattern.

We want to comment on an alternative approach to the present pattern computation. Since the aperture distribution is known over a rectangular grid of sampling points it is tempting to use a FFT to evaluate the aperture integral on the left-hand side of Eq. (10). At the outset of this study we felt that the spatial variations in the aperture distribution would be so slow that a constant amplitude/linear phase approximation would allow a much lower sampling rate than an FFT approach and therefore would be computationally much more efficient. This in fact is the basic idea in the well-known Ludwig algorithm,[2] which uses linear approximation for both the amplitude and phase functions.

At a later stage however, we became interested in the approach of Franceschetti et al,[1] who employ the FFT to compute pattern values at a very sparse set of directions, roughly one value per beamwidth, and then use sinc-functions to interpolate the pattern at in-between directions. Since the pattern is a bandlimited function it follows from sampling theory that this interpolation is highly accurate. In the implementation of this approach we imbedded the sampled original circular aperture distribution in a square one, with zeros filled in over appropriate sections. The side D' of the square was a parameter that we chose slightly larger than the reflector diameter D, since in the FFT this leads to more closely spaced pattern samples and improved accuracy in the interpolation. As will be shown below with the aid of an example, this method of aperture integration is about 20 times faster than the previous method.

A final comment as to the limitations of the aperture field integration method may be in place. Two questions can be distinguished: (a) over how large an angular sector around the reflector axis and (b) over how many sidelobes around the (scanned) main beam can the method be expected to provide reasonably accurate patterns?

These questions are discussed in Appendix C. In regard to the first question it is concluded that out to angles of about $\sqrt{2F/\lambda}$ beamwidths from the reflector axis, the aperture integration method can be considered equivalent to the more accurate reflector current integration method. Thus, for a typical reflector with $D = 100\lambda$ and $F/D = 0.5$, this would indicate a sector of ± 10 beamwidths around the axis. However, our method should give meaningful results over a sector several times larger than this, since we can expect rather graceful accuracy degradation.

To address the second question we compare our method with the Geometrical Theory of Diffraction (GTD) solution for the field diffracted at the reflector edge. The result is that the two methods agree over a region of about $(1/4)D/\lambda$ sidelobes on either side of the main beam. Thus, this number can be considered to be a bound on the number of sidelobes obtainable by the aperture integration

2. Ludwig, A. C. (1968) Computation of radiation patterns involving numerical double integration, IEEE Trans. Antennas Propag. 16:767.

method. Although we feel that this bound may be a bit optimistic, it does serve as an order of magnitude indicator.

3. APERTURE BLOCKAGE

The effects of aperture blockage are readily analyzed since this only requires setting the aperture distribution equal to zero over the blocked region, before the far-field is computed. Presently, provisions are available in the computer program that allow circular or pie-shaped blocked regions.

Frequently however, an order of magnitude estimate of the blockage effect is more convenient. To this end we consider the feed shadow as a field superimposed on the unperturbed far field and compare the radiation intensities in these two fields. These intensities are determined by the power/gain product PG, and therefore the blockage limited sidelobe level

$$L_{block} \simeq \frac{(P \cdot G)_{blockage}}{(P \cdot G)_{aperture}} = \frac{|\rho|^2_{center}}{|\rho|^2_{average}} \frac{A^2_{block}}{\eta A^2_{ap}}$$

$$= \frac{1}{\eta} \frac{|\rho|^2_{center}}{|\rho|^2_{average}} \left(\frac{d}{D}\right)^4 \quad , \tag{12}$$

where d and D denote the feed and the reflector diameter, respectively, η is the aperture efficiency and $|\rho_{center} / \rho_{average}|^2$ is the radiation intensity at the aperture center relative to the average intensity.

For a typical example we choose an aperture distribution $\rho = (1 - r^2)$, corresponding to a pattern with -25 dB sidelobes. In this case $\eta = 0.75$ and $|\rho_{center} / \rho_{average}|^2 = 3$ and therefore,

$$L_{block} = 4\,(d/D)^4 \quad . \tag{13}$$

This relation, which is depicted in Figure 3, shows that in this particular case the blockage sidelobes may be ignored so long as $d/D < 0.15$.

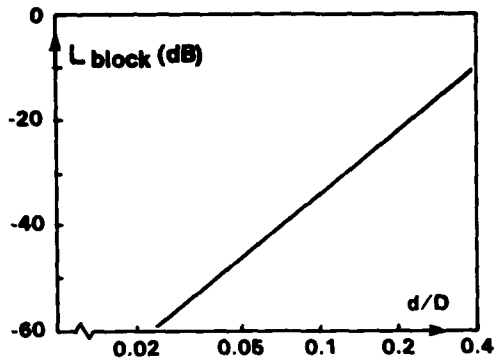

Figure 3. Blockage Limited Sidelobe Level L_{block} vs Feed/Reflector Diameter Ratio d/D

4. ILLUSTRATIVE EXAMPLES OF COMPUTED PATTERNS

In this section we demonstrate the accuracy and the efficiency of the computation method with the aid of a few examples. Only single point feeds are considered since the case of an array feed simply constitutes a superposition of such cases. Patterns shown are computed with the piecewise constant amplitude/linear phase aperture distribution approximation. Computer run times for this approach and the FFT approach are compared in a final paragraph.

As a first case we consider a focal-point fed reflector. The feed has a $1/(1+\cos\theta)$ field pattern which results in a uniform reflector aperture distribution and a far field pattern ideally proportional to $2J_1(x)/x$, where $x = (kD\sin\theta)/2$. Assuming a reflector diameter $D = 200\lambda$ and aperture sample spacing $\tau=4\lambda$ we compute the pattern shown in Figure 4. As can be seen, the sidelobes closely follow the theoretical pattern envelope, which is shown by a dashed line. The differences from the theoretical values are shown in more detail in Table 1, column "Scalar Field". Down to the -30 dB sidelobe level the differences are less than about 0.2 dB, they increase to about 1.5 dB at the -40 dB level. Agreement between theoretical and computed aperture directivity is equally good, the values being 55.96 and 55.99 dB, respectively. This accuracy was considered satisfactory and therefore no patterns were computed with finer aperture sampling, which presumably would have given still better accuracy at the expense of longer computation time.

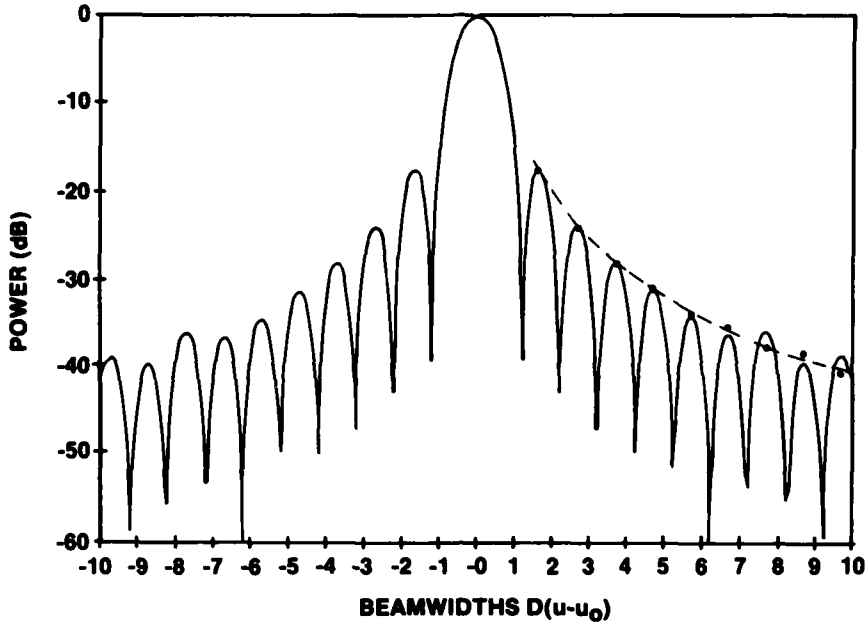

Figure 4. Pattern Computed for a Uniform Aperture D = 200λ With τ = 4λ

To evaluate the quality of our scalar approach to a vector field problem we also computed the vector far-field patterns of this antenna with an independent computer code SAM*,[3] developed by Franceschetti and D'Elia. The code assumes a feed consisting of a balanced Huygens source again with a field form factor $1/(1+\cos\theta)$ and uses reflector current integration. The sidelobes in the E- and H-planes are indicated by circles in Figure 4 and are also given numerically in Table 1. Clearly, for the on-axis case the polarization dependence is small, since the two patterns differ by only 0.01 dB. From this data we infer that the SAM code is highly accurate, so that it can serve as a reference even for off-axis scanned beams.

To evaluate the accuracy degradation with increasing aperture sample spacing τ, we recomputed the patterns using τ = 8λ and τ = 12λ, respectively. The resultant patterns are shown graphically in Figures 5 and 6 and numerically in

*One might ask why we developed an alternative to the SAM code. The two reasons are that (a) its structure is complicated and we were unsuccessful in incorporating an array feed, despite lengthy phone conversations with G. D'Elia in Italy and (b) we felt that the scalar approach would provide acceptable data with less computer run time.

3. Franceschetti, G., and D'Elia, G. (1982) SAM Program. Computer program for offset paraboloidal reflectors, Material from Reflector Antenna Theory, Computation, and Synthesis course, University of Southern California, Los Angeles, Calif.. May 1982.

Table 1. Sidelobe Positions and Amplitudes - Comparison of Scalar and Vector Field Approaches

Sidelobe No.	Theory Ampl (-dB)	Scalar Field			Vector Field, E-plane			Vector Field, H-plane		
		Position (Du)	Ampl (-dB)	Diff (Δ dB)	Position (Du)	Ampl (-dB)	Diff (Δ dB)	Position (Dv)	Ampl (-dB)	Diff (Δ dB)
1	17.59	1.6	17.63	0.04	1.6	17.66	0.07	1.6	17.66	0.07
2	23.81	2.7	23.88	0.07	2.7	23.77	-0.03	2.7	23.77	-0.03
3	27.96	3.7	28.00	0.04	3.7	28.06	0.10	3.7	28.06	0.12
4	31.08	4.7	31.25	0.17	4.7	30.96	-0.12	4.7	30.96	-0.12
5	33.64	5.7	34.44	0.80	5.7	33.80	0.16	5.7	33.79	0.15
6	35.73	6.7	36.62	0.89	6.7	35.50	-0.23	6.7	35.50	-0.23
7	37.53	7.7	36.18	-1.35	7.7	37.83	0.30	7.7	37.82	0.29
8	39.12	8.7	39.90	0.78	8.7	38.81	-0.31	8.7	38.80	-0.32
9	40.53	9.7	39.02	-1.51	9.7	40.96	0.43	9.7	40.95	0.42

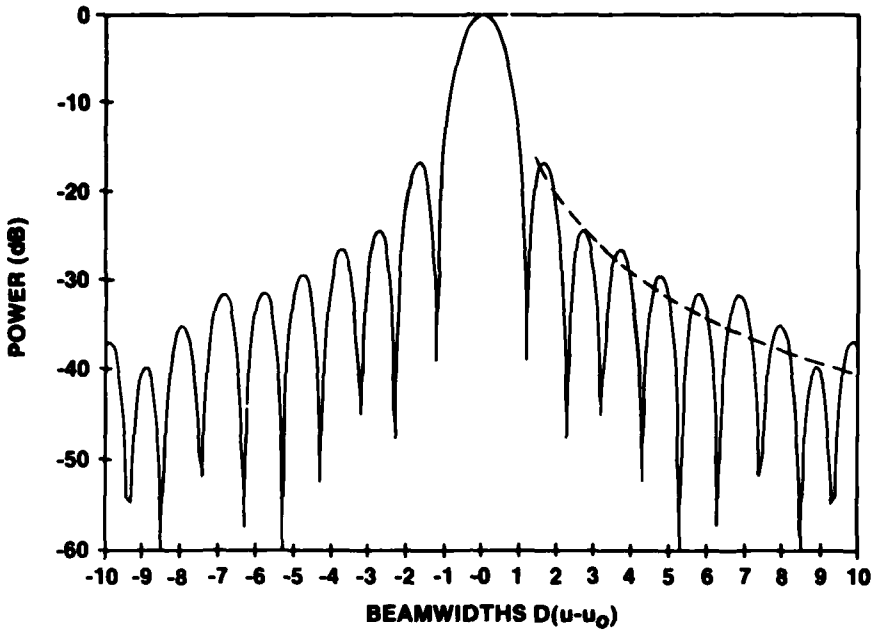

Figure 5. Pattern Computed for a Uniform Aperture With Aperture Sample Spacing Increased From $\tau = 4\lambda$ to $\tau = 8\lambda$

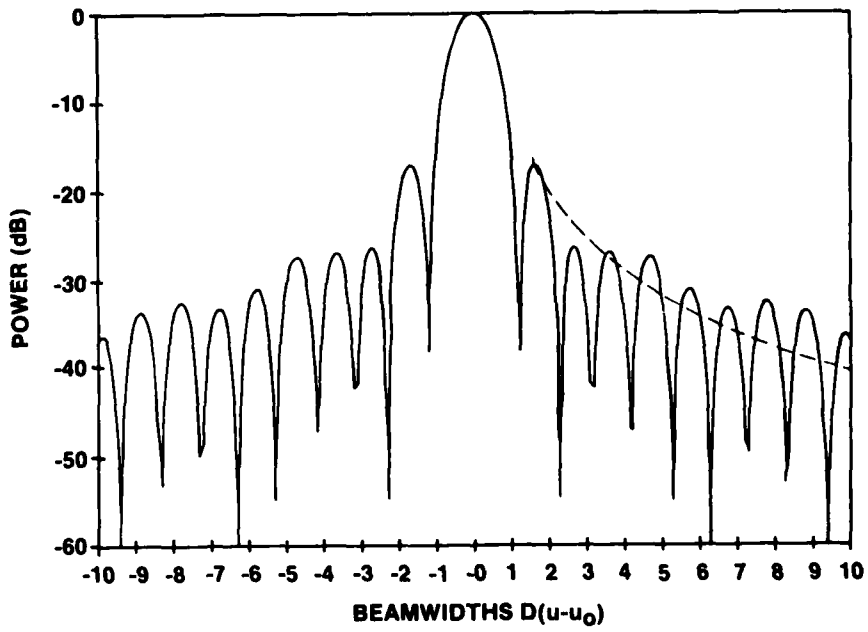

Figure 6. Pattern Computed for a Uniform Aperture With Aperture Sample Spacing Increased to $\tau = 12\lambda$

Table 2. Apparently, the accuracy degrades rapidly even though the present uniform aperture distribution constitutes a particularly simple case, which is perfectly resolved by the constant amplitude/linear phase approximation.

In a second example we scan the beam approximately 10 beamwidths by moving the feed off-axis to a position $x_f = -5.861\lambda$, $y_f = 0$, $z_f = 99.828\lambda$, while keeping it pointing at the reflector center. The feed pattern and reflector remain unchanged. Using again an aperture sample spacing $\tau = 4\lambda$ we obtain the u- and v-plane patterns (through the main beam position $u_o = -0.05$, $v_o = 0$) shown in Figures 7a and 7b. As a reference we also show the sidelobe levels obtained with the SAM code. No distinction between the feed polarization being parallel or orthogonal to the scan plane is made, since this results in differences ≤ 0.03 dB in sidelobe level. A numerical comparison of sidelobes obtained for the scalar and vector field patterns is provided in Tables 3a and 3b. In the u-plane, Table 3a, where no depolarization occurs, we note again good agreement between the two approaches, the difference being ≤ 1 dB for sidelobe levels down to about -30 dB. In the v-plane, Table 3b, we note that depolarization becomes significant. If we compare the pattern of only the dominant θ-polarized field component, we find that the sidelobes are consistently lower than those of the scalar pattern. This is due to the power lost to the ϕ-polarized field component. When we add the powers of these two polarizations, as is done in the column labeled Vector Field, $|E_\theta|^2 + |E_\phi|^2$ in Table 3b, we find much improved agreement with the scalar pattern. The differences are ≤ 0.5 dB down to the -30 dB sidelobe level.

Finally, we illustrate the efficiency of the FFT far-field pattern computation with one representative example. We consider the same reflector, $D = 200\lambda$, $F/D = 0.5$, as before with the beam scanned 10 beamwidths off-axis. The aperture sample spacing $\tau = 4\lambda$ and for the FFT we use 64×64 samples, which makes the zero-filled aperture diameter $D' \simeq 250\lambda$. This choice for D' results in comparable accuracy for the aperture integration methods based on the constant amplitude/linear phase approximation (denoted "subapertures") and on the FFT, respectively. The computer run times for the two methods are compared in Table 4, which lists seconds of CP-time on a CDC Cyber 750 computer. Time for the 64×64 FFT alone is about 0.6 sec CP-time, which shows that 50 percent of the time is used for the pattern interpolation.

Table 2. Sidelobe Positions and Amplitudes - Dependence on Aperture Sample Spacing τ

Sidelobe No.	Theory Ampl (-dB)	$\tau = 4\ \lambda$			$\tau = 8\ \lambda$			$\tau = 12\ \lambda$		
		Position (Du)	Ampl (-dB)	Diff (Δ dB)	Position (Du)	Ampl (-dB)	Diff (Δ dB)	Position (Du)	Ampl (-dB)	Diff (Δ dB)
1	17.6	1.6	17.6	0.0	1.6	16.9	-0.7	1.6	17.2	-0.4
2	23.8	2.7	23.9	-0.1	2.7	24.4	0.6	2.7	26.3	2.5
3	28.0	3.7	28.0	0.0	3.7	26.6	-1.4	3.6	26.8	-1.2
4	31.1	4.7	31.3	0.2	4.8	29.5	-1.6	4.7	27.3	-3.8
5	33.6	5.7	34.4	0.8	5.8	31.4	-2.2	5.8	30.9	-2.7
6	35.7	6.7	36.6	0.9	6.9	31.8	-3.9	6.8	33.2	-3.5
7	37.5	7.7	36.2	-1.3	7.9	35.2	-2.3	7.8	32.4	-5.1
8	39.1	8.7	39.9	0.8	8.9	39.8	0.7	8.9	33.6	-5.5
9	40.5	9.7	39.0	-1.5	9.9	36.9	-3.6	9.9	36.4	-4.1
Gain (dB)	55.96	55.99			55.90			55.92		

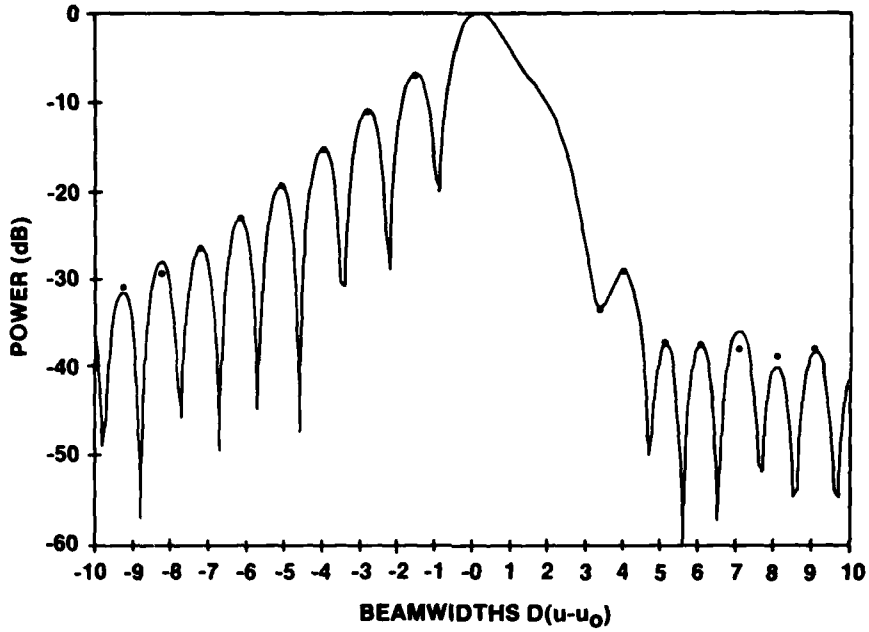

Figure 7a. Pattern in the u-plane Through the Main Beam at u_o=0.05, v_o=0

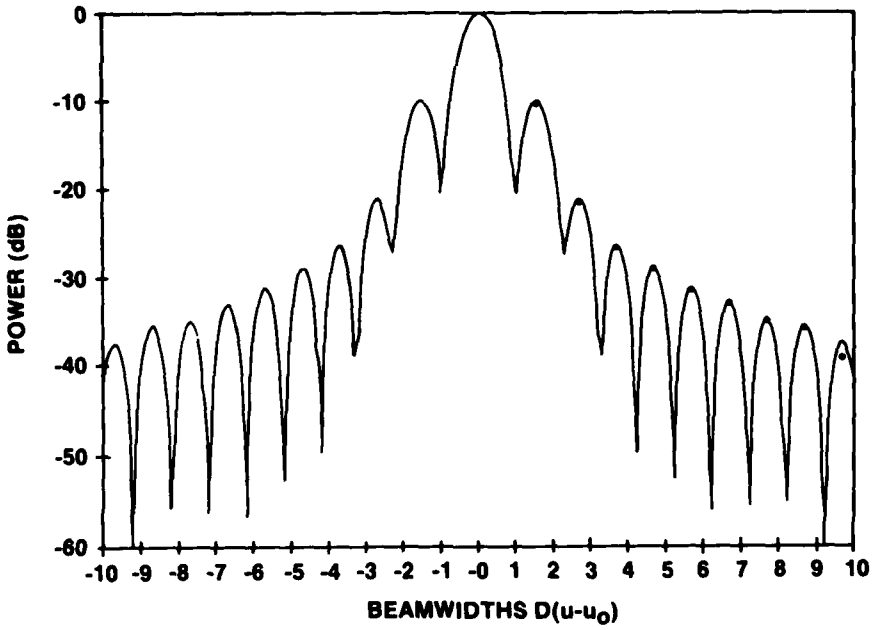

Figure 7b. Pattern in the v-plane Through the Main Beam at u_o=0.05, v_o=0

Table 3a. Sidelobe Positions and Amplitudes in u-plane Cut Through Main Beam - Comparison of Scalar and Vector Field Approaches. Main beam scanned to $u_o = 0.05$, $v_o = 0$

Sidelobe No.	Scalar Field		Vector Field		Diff (Δ dB)
	Position $[D(u-u_o)]$	Ampl (-dB)	Position $[D(u-u_o)]$	Ampl (-dB)	
-8	-9.3	31.3	-9.3	31.0	-0.3
-7	-8.2	28.0	-8.3	29.0	1.0
-6	-7.2	26.1	-7.2	26.2	0.1
-5	-6.2	23.2	-6.2	23.1	-0.1
-4	-5.1	19.3	-5.1	19.4	0.1
-3	-4.0	15.2	-4.0	15.5	0.3
-2	-2.8	10.9	-2.8	11.1	0.2
-1	-1.5	6.8	-1.6	7.1	0.3
main beam	0	0	0	0	0
1	4.0	29.1	4.0	29.0	-0.1
2	5.1	37.4	5.1	36.0	-1.4
3	6.1	37.5	6.1	35.9	-1.6
4	7.1	35.8	7.1	38.2	2.4
5	8.1	40.1	8.1	38.6	-1.5
6	9.1	38.3	9.1	40.7	2.4

Table 3b. Sidelobe Positions and Amplitudes in v-plane Cut Through Main Beam - Comparison of Scalar and Vector Field Approaches. Main beam scanned to $u_o = 0.05$, $v_o = 0$

Sidelobe No.	Scalar Field		Vector Field, $\|E_\theta\|^2$ Only			Vector Field, $\|E_\theta\|^2 + \|E_\phi\|^2$		
	Position (Dv)	Ampl (-dB)	Position (Dv)	Ampl (-dB)	Diff (Δ dB)	Position (Dv)	Ampl (-dB)	Diff (Δ dB)
1	1.5	10.0	1.5	10.6	0.5	1.5	10.4	0.4
2	2.7	21.0	2.7	21.8	0.8	2.7	21.5	0.5
3	3.7	26.2	3.7	27.0	0.7	3.7	26.5	0.3
4	4.7	28.8	4.7	29.5	0.7	4.7	28.7	-0.1
5	5.7	31.0	5.7	32.4	1.4	5.7	31.2	0.2
6	6.7	32.8	6.7	34.3	1.5	6.7	32.7	-0.1
7	7.7	34.8	7.7	36.9	2.1	7.7	34.9	0.1
8	8.7	35.4	8.7	38.3	2.9	8.7	35.8	0.4
9	9.7	37.3	9.7	40.8	3.5	9.7	39.4	2.1

Table 4. Computer Time for One Pattern Cut Over 20 Beamwidths

Number of Pattern Points	Time for Aperture Distribution	Total Run Time		Pattern Integration Time		FFT Time Reduction Factor
		Subaperture	FFT	Subaperture	FFT	
200	11.5	35.0	12.8	23.5	1.3	18

5. CONCLUSIONS

We have developed a simple and efficient computational method for the evaluation of reflector antenna patterns. The method is useful in situations where a large number of candidate antenna configurations has to be analyzed, as is the case when synthesizing an antenna to a given design goal or when scoping a reflector limited scan technique.

The three essential features of the approach are (a) the use of ray optics to map the off-axis feed onto the reflector aperture, (b) the use of Fermat's principle to determine the ray path from the feed to a given point on the aperture, and (c) the use of a rectangular aperture sampling grid and FFT to speed up the pattern integration. The pattern and the absolute gain are determined for arbitrary feed locations and orientations, the only restriction being that the reflector lies entirely in the Fraunhofer region of the feed. Expressions have been derived for the far field feed array pattern corresponding to two different feed array elements: idealized cos θ-elements and mutually coupled, circular waveguide elements.

Patterns computed by the aperture field integration method compare well with known analytic results and with patterns computed independently with the SAM code, which is based on reflector current integration. The validity of the aperture integration method is further discussed in an appendix, where it is compared with integration over the actual reflector surface and with the GTD solution. A present limitation lies in the scalar field formulation, which neglects the cross polarization. However, the latter can be easily incorporated using simple geometrical polarization factors, such as derived in Reference 4.

4. Kauffman, J.F., Croswell, W.F., and Jowers, L.J. (1976) Analysis of the radiation patterns of reflector antennas, IEEE Trans. Antennas Propag. 24:53.

References

1. Bucci, O.M., Franceschetti, G., and D'Elia, G. (1980) Fast analysis of large antennas - A new computational philosophy, IEEE Trans. Antennas Propag. 28:306.
2. Ludwig, A.C. (1968) Computation of radiation patterns involving numerical double integration, IEEE Trans. Antennas Propag. 16:767.
3. Franceschetti, G., and D'Elia, G. (1982) SAM Program. Computer program for offset paraboloidal reflectors, Material from Reflector Antenna Theory, Computation, and Synthesis course, University of Southern California, Los Angeles, Calif., May 1982.
4. Kauffman, J.F., Croswell, W.F., and Jowers, L.J. (1976) Analysis of the radiation patterns of reflector antennas, IEEE Trans. Antennas Propag. 24:53.

Appendix A

Feed Array Pattern

In this section we derive the scalar far-field pattern f of the feed array. The main difficulty is the proper normalization such that $|f(\theta,\phi)|^2$ represents the directivity in the direction (θ,ϕ).* Two types of array elements, idealized cos θ-elements and realistic circular waveguide elements, will be considered.

We assume that the far field of the single, isolated feed element with excitation V can be expressed as

$$\bar{E}_o(r,\theta,\phi) = V(e_{o\theta}\,\hat{\theta} + e_{o\phi}\,\hat{\phi})\, e^{j\psi} \cdot e^{-jkr}/r \quad , \tag{A1}$$

where $e_{o\theta} = e_{o\theta}(\theta,\phi)$, $e_{o\phi} = e_{o\phi}(\theta,\phi)$ are real functions, $\hat{\theta}$ and $\hat{\phi}$ are unit vectors, ψ represents a constant phase angle, and e^{-jkr}/r represents the spherical wavefront. Consequently, for an N-element array with excitation coefficients $\{V_n\}_1^N$ the far field is

$$\bar{E} = (e_{o\theta}\,\hat{\theta} + e_{o\phi}\,\hat{\phi})\, e^{j\psi}\, (e^{-jkr}/r) \sum_n V_n\, e^{jk\hat{r}\cdot\bar{r}_n} \quad , \tag{A2}$$

*Note that in this appendix r, θ, ϕ stand for the spherical coordinates in the local feed coordinate system, which in the main text carries a prime sign.

where $\hat{r} = (\sin\theta\cos\phi, \sin\theta\sin\phi, \cos\theta)$ is the unit vector in the observation direction (θ, ϕ) and $\bar{r}_n$ is the position vector of the n:th element, see Figure A1. From Eq. (A2) we derive a scalar field E, which correctly describes the field magnitude and phase but suppresses the polarization, as required for our ray analysis, by setting

$$E = e_o \left(e^{-jkr_o}/r_o\right) \sum_n V_n e^{jk\hat{r}\cdot\bar{r}_n} \quad , \tag{A3a}$$

where

$$e_o(\theta, \phi) = \sqrt{e_{o\theta}^2 + e_{o\phi}^2}\; e^{j\psi} \quad . \tag{A3b}$$

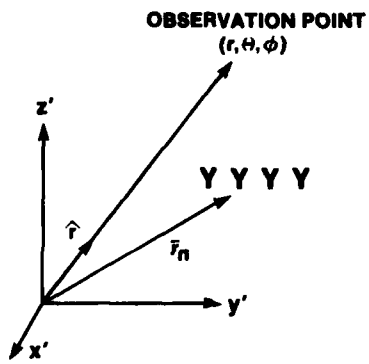

Figure A1. Feed Coordinate System

The desired scalar far-field pattern $f(\theta, \phi)$ is now defined by the conditions:

$|f(\theta, \phi)|^2$ = directivity in direction (θ, ϕ),

$$\arg f = \arg\left[e_o \Sigma V_n e^{jk\hat{r}\cdot\bar{r}_n}\right] \quad , \tag{A4}$$

which leads to

$$f(\theta,\phi) = \frac{\sqrt{2\pi}\, e_o\, \Sigma\, V_n\, e^{jk\hat{r}\cdot\bar{r}_n}}{\left[\int |e_o\, \Sigma\, V_n\, e^{jk\hat{r}\cdot\bar{r}_n}|^2\, d\Omega\right]^{1/2}} \tag{A5a}$$

or alternatively

$$f(\theta,\phi) = \left[\frac{4\pi\, Y_o}{P_{rad}}\right]^{1/2} e_o\, \Sigma\, V_n\, e^{jk\hat{r}\cdot\bar{r}_n} \quad , \tag{A5b}$$

where Y_o is the free space admittance and

$$P_{rad} = \int_{4\pi} Y_o\, |E|^2\, r^2\, d\Omega \tag{A6}$$

denotes the total power radiated by the feed array.

A1. IDEALIZED ARRAY ELEMENT

In this case the array element pattern is

$$e_o(\theta,\phi) = \begin{cases} \sqrt{\cos\theta} & \theta \le \pi/2 \\ 0 & \theta > \pi/2 \end{cases} \tag{A7}$$

and the only difficulty lies in the evaluation of the integral,

$$I = \int_{4\pi} \left|e_o \sum_{n=1}^{N} V_n\, e^{jk\hat{r}\cdot\bar{r}_n}\right|^2 d\Omega \tag{A8}$$

in the denominator of Eq. (A5a).

Substitution of Eq. (A7) in Eq. (A8) and expansion of the square leads to a double sum

$$I = \sum_{m=1}^{N} \sum_{n=1}^{N} T_{mn} \quad , \tag{A9a}$$

where each term is given by

$$T_{mn} = V_m V_n^* \int_0^{\pi/2} \int_0^{2\pi} \cos\theta \, e^{jk\hat{r}\cdot(\bar{r}_m - \bar{r}_n)} \sin\theta \, d\theta \, d\phi$$

$$= V_m V_n^* \int_0^{\pi/2} \int_0^{2\pi} e^{jk[(x_m - x_n)\cos\phi + (y_m - y_n)\sin\phi]\sin\theta} \sin\theta \cos\theta \, d\theta \, d\phi \tag{A9b}$$

and the asterisk denotes comples conjugate.

Equation (A9b) can be integrated analytically and the result is

$$T_{mn} = \begin{cases} V_m V_n^* \dfrac{2\pi}{ks_{mn}} J_1(ks_{mn}) & m \neq n \\ |V_m|^2 \pi & m = n \end{cases} , \tag{A10}$$

where

$$s_{mn} = s_{nm} = [(x_m' - x_n')^2 + (y_m' - y_n')^2]^{1/2} \tag{A11}$$

is the distance between element m and element n, and J_1 denotes the Bessel function of the first kind and order 1. Thus, for $\cos\theta$-elements the field pattern for the feed array is

$$f(\theta, \phi) = \left[\frac{4\pi \cos\theta}{\sum_m \sum_n T_{mn}} \right]^{1/2} \sum_n V_n e^{jk(x_n' \cos\phi + y_n' \sin\phi)\sin\theta} , \tag{A12}$$

where the terms T_{mn} are given by Eq. (A10).

A2. CIRCULAR WAVEGUIDE ELEMENTS

In this case the feed consists of an array of open-ended circular, dielectric loaded waveguides in a ground plane. Each waveguide is matched to its (single element) radiation admittance and is assumed to be driven in the dominant mode by a matched generator.

The desired pattern function $f(\theta, \phi)$ is now derived in the following way. The aperture field of each waveguide is approximated by the two orthogonal dominant modes, one driven and one parasitic. Ideally, the aperture excitation of each guide and, consequently, the radiated field is directly proportional to its driving generator voltage. In a realistic array however, the aperture excitation will be perturbed by the mutual coupling between the elements. We evaluate this effect with the aid of a separate computer code based on Reference A1 with cylinder radius $\rightarrow \infty$, which for a given set of N elements driven with voltages $\{A_n\}_1^N$ computes perturbed driven aperture voltages $\{V_n'\}_1^N$ and reflected mode amplitudes $\{R_n'\}_1^N$ and corresponding quantities $\{V_n''\}_1^N$ and $\{R_n''\}_1^N$ for the parasitic mode, see Figure A2.

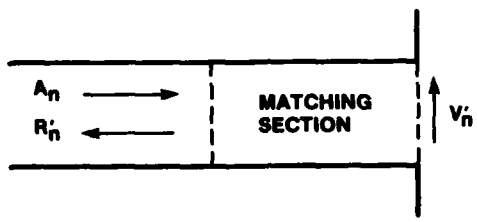

Figure A2. Waveguide Element With Aperture Matching Section

The explicit form for the y-polarized TE11-mode function $\overline{\phi}(r, \phi) = \phi_r \hat{r} + \phi_\phi \hat{\phi}$ is

$$\phi_r = \frac{1}{J_1(x)} \left[\frac{2/\pi}{x^2-1}\right]^{1/2} \frac{1}{r} J_1\left(\frac{xr}{a}\right) \sin\phi$$

$$\phi_\phi = \frac{1}{J_1(x)} \left[\frac{2/\pi}{x^2-1}\right]^{1/2} \frac{x}{a} J_1'\left(\frac{xr}{a}\right) \cos\phi$$

$$x \simeq 1.841 \quad , \tag{A13}$$

where a is the guide radius.

The far field $\overline{E} = E_{o\theta}\hat{\theta} + E_{o\phi}\hat{\phi}$ radiated from an electric aperture field $V'\overline{\phi}$ is[A1]

A1. Steyskal, H. (1977) Analysis of circular waveguide arrays on cylinders, IEEE Trans. Antennas Propag. 25:610.

$$E_{o\theta} = j\,V'\,(e^{-jkr}/r)\left[\frac{2/\pi}{x^2-1}\right]^{1/2}\frac{\sin\phi}{\sin\theta}\,J_1\,(ka\,\sin\theta)$$

$$E_{o\phi} = j\,V'\,(e^{-jkr}/r)\left[\frac{2/\pi}{x^2-1}\right]^{1/2}\frac{ka\cos\theta\cos\phi}{1-\left(\frac{ka\sin\theta}{x}\right)^2}\,J_1'\,(ka\,\sin\theta)\quad . \tag{A14}$$

By comparison of Eq. (A14) with Eq. (A3b), we deduce the scalar element pattern to be

$$e_o^{(y)} = j\left[\frac{2/\pi}{x^2-1}\right]^{1/2} ka\left[\left(\sin\phi\,\frac{J_1(ka\,\sin\theta)}{ka\,\sin\theta}\right)^2 + \left(\cos\theta\,\cos\phi\,\frac{J_1'(ka\,\sin\theta)}{1-\left(\frac{ka\,\sin\theta}{x}\right)^2}\right)^2\right]^{1/2}\quad , \tag{A15}$$

where the superscript (y) indicates that this pattern corresponds to the y-polarized TE11-mode. The pattern for the x-polarized TE11-mode is

$$e_o^{(x)} = j\left[\frac{2/\pi}{x^2-1}\right]^{1/2} ka\left[\left(\cos\phi\,\frac{J_1(ka\,\sin\theta)}{ka\,\sin\theta}\right)^2 + \left(\cos\theta\,\sin\phi\,\frac{J_1'(ka\,\sin\theta)}{1-\left(\frac{ka\,\sin\theta}{x}\right)^2}\right)^2\right]^{1/2}\quad , \tag{A16}$$

which is obtained from Eq. (A15) by a simple interchange of $\sin\phi$ and $\cos\phi$.

For the proper normalization of the feed pattern f we also must determine the total power radiated by the array. This could again be done by integrating the pattern over 4π sr, but fortunately this time there is a simpler method. The power incident at the waveguide apertures is

$$P_i = Y_{TE11}\sum_n |A_n|^2 \tag{A17}$$

and the power reflected is

$$P_r = Y_{TE11} \sum_n (|R_n'|^2 + |R_n''|^2) \quad , \tag{A18}$$

where Y_{TE11} denotes the TE11-mode admittance. The difference must be the radiated power and therefore,

$$P_{rad} = Y_{TE11} \sum_n (|A_n|^2 - |R_n'|^2 - |R_n''|^2) \quad . \tag{A19}$$

The scalar field pattern now becomes

$$f = [4\pi\, Y_o/P_{rad}]^{1/2}\, e_o \sum_n A_n\, e^{jk(x_n' \cos\phi + y_n' \sin\phi)\cos\theta} \quad , \tag{A20}$$

where P_{rad} is given by Eq. (A19) and the element pattern

$$e_o = \begin{cases} e_o^{(x)} & \text{for x-polarized excitation} \\ e_o^{(y)} & \text{for y-polarized excitation} \end{cases}$$

is given by Eqs. (A15) and (A16).

Appendix B

Feed-Aperture Mapping

In this section we determine the relation between the solid angle cross-section $d\Omega$ of a ray tube, which emanates from the feed, and the area dA, which this ray tube intercepts at the aperture, see Figure B1. This is a purely geometrical problem and we repeat the defining equations here before we develop the solution.

(1) Paraboloid equation	$x^2 + y^2 = 4Fz$	(B1)
(2) Focal length	F	
(3) Reflector diameter	D	
(4) Given ray origin point	(x_f, y_f, z_f)	
Known reflection point	(x_r, y_r, z_r)	determined from Eq. (B2) below.
Given aperture intercept point	(x_a, y_a, z_a)	

(5) Feed-reflector distance

$$s_f = \left[(x_r - x_f)^2 + (y_r - y_f)^2 + \left(\frac{x_r^2 + y_r^2}{4F} - z_f \right)^2 \right]^{1/2}$$

(6) Reflector-aperture distance

$$s_a = \left[(x_r - x_a)^2 + (y_r - y_a)^2 + \left(\frac{x_r^2 + y_r^2}{4F} - z_a \right)^2 \right]^{1/2}$$

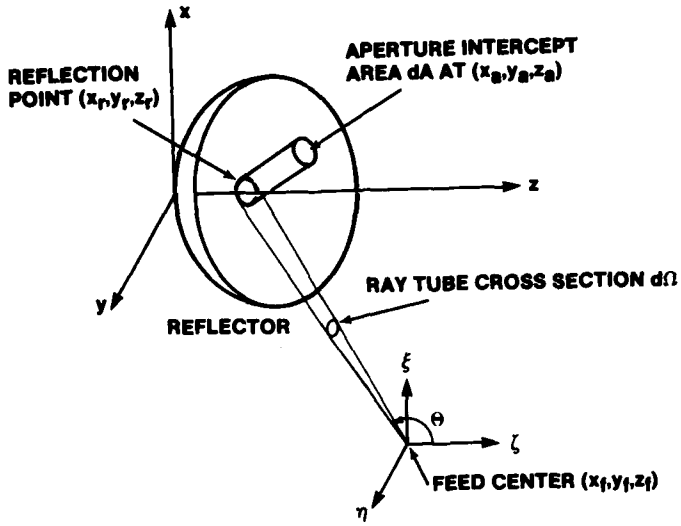

Figure B1. Ray Trajectory From Feed to Aperture

(7) Total ray path length $\qquad s = s_f + s_a = \text{minimum} \quad , \qquad$ (B2)

with respect to x_r, y_r, (Fermat's principle).

We also introduce a local, feed-centered coordinate system ξ, η, ζ, which is translated relative to the system x, y, z,

$$\xi = x - x_f$$

$$\eta = y - y_f$$

$$\zeta = z - z_f \quad , \qquad \text{(B3)}$$

since in this system the ray tube cross-section $d\Omega$ is conveniently expressed as

$$d\Omega = |\sin\theta \, d\theta \, d\phi| \quad , \qquad \text{(B4)}$$

where θ and ϕ are the local spherical coordinates.*

The desired relation between the solid angle $d\Omega$ and the aperture element dA is now obtained as follows. We consider the coordinates θ, ϕ that determine

*Note that in this appendix the spherical angles θ, ϕ are different from those in Appendix A, since the ξ, η, ζ-system here is rotated relative to the x, y, z-system.

the ray direction, to be functions of the coordinates x_a, y_a at which the ray intercepts the aperture,

$$\theta = \theta(x_a, y_a)$$

$$\phi = \phi(x_a, y_a) \quad . \tag{B5}$$

The mapping of an aperture area element $dx_a\, dy_a$ onto an element $d\theta\, d\phi$ is given by

$$d\theta\, d\phi = J\, dx_a\, dy_a \quad , \tag{B6}$$

where the Jacobian

$$J = \frac{\partial\theta}{\partial x_a}\frac{\partial\phi}{\partial y_a} - \frac{\partial\theta}{\partial y_a}\frac{\partial\phi}{\partial x_a} \quad . \tag{B7}$$

Substituting Eq. (B4) in Eq. (B6) and setting $dA = |dx_a\, dy_a|$ yields the desired relation

$$\frac{d\Omega}{dA} = |J| \sin\theta \quad , \tag{B8a}$$

where

$$\sin\theta = \left[\frac{\xi_r^2 + \eta_r^2}{\xi_r^2 + \eta_r^2 + \zeta_r^2}\right]^{1/2} = \left[(x_r - x_f)^2 + (y_r - y_f)^2\right]^{1/2} \Big/ s_f \quad . \tag{B8b}$$

This completes the derivation of $d\Omega/dA$. The remainder of this appendix will be devoted to the development of explicit expressions for the partial derivatives in the Jacobian.

According to Fermat's principle Eq. (B2) the reflection point (x_r, y_r, z_r) is a stationary point so that

$$\frac{\partial s}{\partial x_r} = 0$$

$$\frac{\partial s}{\partial y_r} = 0 \quad . \tag{B9}$$

For small position increments dx_a, dy_a in the aperture point the resulting increments dx_r, dy_r in the reflection point will be such that Eq. (B9) still holds, that is,

$$d\left(\frac{\partial s}{\partial x_r}\right) = \frac{\partial^2 s}{\partial x_r^2}\, dx_r + \frac{\partial^2 s}{\partial y_r \partial x_r}\, dy_r + \frac{\partial^2 s}{\partial x_a \partial x_r}\, dx_a + \frac{\partial^2 s}{\partial y_a \partial x_r}\, dy_a = 0$$

$$d\left(\frac{\partial s}{\partial y_r}\right) = \frac{\partial^2 s}{\partial x_r \partial y_r}\, dx_r + \frac{\partial^2 s}{\partial y_r^2}\, dy_r + \frac{\partial^2 s}{\partial x_a \partial y_r}\, dx_a + \frac{\partial^2 s}{\partial y_a \partial y_r}\, dy_a = 0 \quad . \qquad \text{(B10)}$$

From Eq. (B10) we solve for dx_r, dy_r in terms of dx_a, dy_a to obtain

$$dx_r = \alpha\, dx_a + \beta\, dy_a$$

$$dy_r = \gamma\, dx_a + \delta\, dy_a \quad , \qquad \text{(B11)}$$

where

$$\alpha = \frac{1}{C}\left[\frac{\partial^2 s}{\partial y_r \partial x_r}\,\frac{\partial^2 s}{\partial x_a \partial y_r} - \frac{\partial^2 s}{\partial y_r^2}\,\frac{\partial^2 s}{\partial x_a \partial x_r}\right]$$

$$\beta = \frac{1}{C}\left[\frac{\partial^2 s}{\partial y_r \partial x_r}\,\frac{\partial^2 s}{\partial y_a \partial y_r} - \frac{\partial^2 s}{\partial y_r^2}\,\frac{\partial^2 s}{\partial y_a \partial x_r}\right]$$

$$\gamma = \frac{1}{C}\left[\frac{\partial^2 s}{\partial x_r \partial y_r}\,\frac{\partial^2 s}{\partial x_a \partial x_r} - \frac{\partial^2 s}{\partial x_r^2}\,\frac{\partial^2 s}{\partial x_a \partial y_r}\right]$$

$$\delta = \frac{1}{C}\left[\frac{\partial^2 s}{\partial x_r \partial y_r}\,\frac{\partial^2 s}{\partial y_a \partial x_r} - \frac{\partial^2 s}{\partial x_r^2}\,\frac{\partial^2 s}{\partial y_a \partial y_r}\right] \qquad \text{(B12a)}$$

with

$$C = \frac{\partial^2 s}{\partial x_r^2}\,\frac{\partial^2 s}{\partial y_r^2} - \left(\frac{\partial^2 s}{\partial x_r \partial y_r}\right)^2 \quad . \qquad \text{(B12b)}$$

The derivation of explicit expressions for the second-order partial derivatives of $s=s_f+s_a$ required for α, β, γ, δ is lengthy but straightforward. The result is

$$\frac{\partial^2 s}{\partial x_r^2} = [1 + (z_r-z_f)/2F + x_r^2/4F^2]/s_f - [x_r-x_f + x_r(z_r-z_f)/2F]^2/s_f^3 +$$

$$+ [1 + (z_r-z_a)/2F + x_r^2/4F]/s_a - [x_r-x_a + x_r(z_r-z_a)/2F]^2/s_a^3$$

$$\frac{\partial^2 s}{\partial x_r \partial y_r} = x_r y_r(1/s_f+1/s_a)/4F^2 - [x_r-x_f + x_r(z_r-z_f)/2F] \cdot$$

$$\cdot [y_r-y_f + y_r(z_r-z_f)/2F]/s_f^3 - [x_r-x_a + x_r(z_r-z_a)/2F] \cdot$$

$$\cdot [y_r-y_a + y_r(z_r-z_a)/2F]/s_a^3$$

$$\frac{\partial^2 s}{\partial y_r^2} = [1 + (z_r-z_f)/2F + y_r^2/4F^2]/s_f - [y_r-y_f + y_r(z_r-z_f)/2F]^2/s_f^3 +$$

$$+ [1 + (z_r-z_a)/2F + y_r^2/4F^2]/s_f - [y_r-y_a + y_r(z_r-z_a)/2F]^2/s_a^3$$

$$\frac{\partial^2 s}{\partial x_a \partial x_r} = -1/s_a + (x_r-x_a)[x_r-x_a + x_r(z_r-z_a)/2F]/s_a^3$$

$$\frac{\partial^2 s}{\partial x_a \partial y_r} = (x_r-x_a)[y_r-y_a + y_r(x_r^2 + y_r^2 - 4F z_a)/8F^2]/s_a^3$$

$$\frac{\partial^2 s}{\partial y_a \partial x_r} = (y_r-y_a)[x_r-x_a + x_r(x_r^2 + y_r^2 - 4F z_a)/8F^2]/s_a^3$$

$$\frac{\partial^2 s}{\partial y_a \partial y_r} = -1/s_a + (y_r-y_a)[y_r-y_a + y_r(z_r-z_a)/2F]/s_a^3 \quad . \qquad \text{(B13)}$$

Returning to Eq. (B11), we note that the coordinate increments dx_r, dy_r on the reflector surface also are accompanied by an increment

$$dz_r = (x_r dx_r + y_r dy_r)/2F \quad . \tag{B14}$$

We have now traced the aperture point increments dx_a, dy_a to corresponding reflection-point increments dx_r, dy_r, dz_r and it now only remains for determine how these increments are viewed from the feed in terms of $d\theta$, $d\phi$. In other words, we need to determine the unknown coefficients in the relation

$$d\theta = a_1\, dx_r + a_2\, dy_r + a_3\, dz_r$$

$$d\phi = b_1\, dx_r + b_2\, dy_r + b_3\, dz_r \quad . \tag{B15}$$

Once we have these coefficients we can substitute Eqs. (B11) and (B14) in Eq. (B15) to obtain

$$d\theta = c_1\, dx_a + c_2\, dy_a$$

$$d\phi = c_3\, dx_a + c_4\, dy_a \quad , \tag{B16}$$

where the four new coefficients c_1, c_2, c_3, c_4 now can be identified as the four partial derivatives required for the Jacobian. Thus, we have

$$\frac{\partial\theta}{\partial x_a} = c_1 = \alpha(a_1 + a_3 x_r/2F) + \gamma(a_2 + a_3 y_r/2F)$$

$$\frac{\partial\theta}{\partial y_a} = c_2 = \beta(a_1 + a_3 x_r/2F) + \delta(a_2 + a_3 y_r/2F)$$

$$\frac{\partial\phi}{\partial x_a} = c_3 = \alpha(b_1 + b_3 x_r/2F) + \gamma(b_2 + b_3 y_r/2F)$$

$$\frac{\partial\phi}{\partial y_a} = c_4 = \beta(b_1 + b_3 x_r/2F) + \delta(b_2 + b_3 y_r/2F) \quad . \tag{B17}$$

The coefficients $a_1, a_2, a_3, b_1, b_2, b_3$ are determined as follows. From the standard relation between spherical and rectangular coordinates

$$\cos\theta = \frac{\zeta}{\sqrt{\xi^2+\eta^2+\zeta^2}} = \frac{\zeta}{s_f}$$

$$\cos\phi = \frac{\xi}{\sqrt{\xi^2+\eta^2}} = \frac{\xi}{t} \tag{B18}$$

we obtain by differentiation

$$d\theta = [\xi\zeta\, d\xi + \eta\zeta\, d\eta - t^2\, d\zeta]/s_f^2\, t$$

$$d\phi = [-\eta\, d\xi + \xi\, d\eta]/t^2 \quad , \tag{B19}$$

where

$$t = \sqrt{\xi^2 + \eta^2} \quad . \tag{B20}$$

In view of Eq. (B3) we have

$$d\xi = dx,\ d\eta = dy,\ d\zeta = dz \tag{B21}$$

and when we substitute Eq. (B21) in Eq. (B19) and identify the resulting expression with Eq. (B15) we find

$$a_1 = \xi_r \zeta_r / s_f^2\, t_r \qquad b_1 = -\eta_r / t_r^2$$

$$a_2 = \eta_r \zeta_r / s_f^2\, t_r \qquad b_2 = \xi_r / t_r^2$$

$$a_3 = -t_r / s_f^2 \qquad b_3 = 0 \quad , \tag{B22}$$

where the subscript r indicates that the value at the reflection point is to be used.

Substitution of Eqs. (B3) and (B22) in Eq. (B17) yields

$$\frac{\partial\theta}{\partial x_a} = \{\alpha[(x_r-x_f)(z_r-z_f) - x_r t_r^2/2F] + \gamma[(y_r-y_f)(z_r-z_f) - y_r t_r^2/2F]\}/s_f^2 t_r$$

$$\frac{\partial\theta}{\partial y_a} = \{\beta[(x_r-x_f)(z_r-z_f) - x_r t_r^2/2F] + \delta[(y_r-y_f)(z_r-z_f) - y_r t_r^2/2F]\}/s_f^2 t_r$$

$$\frac{\partial\phi}{\partial x_a} = [-\alpha(y_r-y_f) + \gamma(x_r-x_f)]/t_r^2$$

$$\frac{\partial\phi}{\partial y_a} = [-\beta(y_r-y_f) + \delta(x_r-x_f)]/t_r^2 \quad , \tag{B23a}$$

where

$$t_r = \sqrt{(x_r-x_f)^2 + (y_r-y_f)^2} \quad . \tag{B23b}$$

In summary, we have now, via Eqs. (B8), (B7), (B23), (B12), and (B13), expressed the desired function $d\Omega/dA$ entirely in terms of the known coordinates of the feed point, reflection point, and aperture intercept point.

Appendix C

Validity of the Aperture Integration Method

We want to briefly comment on the validity of the patterns obtained by the aperture integration method. In particular, we want to know over how large an angular sector around the reflector axis the method is valid and how many sidelobes about the (scanned) beam are accurately predicted.

The first question may be answered by comparing our method of integrating over an equivalent planar aperture with a more accurate integration over the actual, curved reflector surface. This is done in Reference C1, where it is shown that the two methods are equivalent out to angles in the order of $\sqrt{2F/\lambda}$ times the beamwidth. For larger angles there will be quantitative differences, although we would still expect good qualitative agreement.

One numerical example illustrating this point is provided by the patterns of Table 3. There, good agreement between the aperture field integration and current integration methods is shown out to 19 beamwidths from the reflector axis, which is 1.4 times further than the 14 beamwidths obtained by the $\sqrt{2F/\lambda}$-criterion.

The conservativeness of this criterion is further demonstrated in the next example, where it is exceeded by a factor of 3. We consider a reflector with $D = 100\lambda$, $F/D = 0.5$, with a balanced Huygens feed located at $x_f = -9.98\lambda$, $y_f = 0$, $z_f = 49.08\lambda$, and with a $1/(1+\cos\theta)$ field pattern pointing at the reflector center.

C1. Clarke, R.H., and Brown, J. (1980) Diffraction Theory and Antennas, John Wiley & Sons, N.Y., p. 196-199.

The nominal main-beam position is $u_o = 0.174$, $v_o = 0$, corresponding to a scan angle of about 17.4 beamwidths. The u-plane pattern through the main beam obtained with the aperture integration method is shown in Figure C1. The sidelobe magnitudes and positions as computed with the current integration method (SAM) are indicated by circles in the same figure. The maximum difference is 2.7 dB and clearly the two methods produce very similar patterns out to at least 27 beamwidths from the axis. The $\sqrt{2F/\lambda}$ -criterion yields only 10 beamwidths in this case. The corresponding v-plane patterns through the main beam agree with the same accuracy as in the u-plane pattern when the powers of the θ- and ϕ-polarized components are combined. Computations with two orthogonal feed polarizations showed that the patterns are very insensitive in this regard, since the sidelobe peak variations were less than 0.01 dB down to the -40 dB sidelobe level.

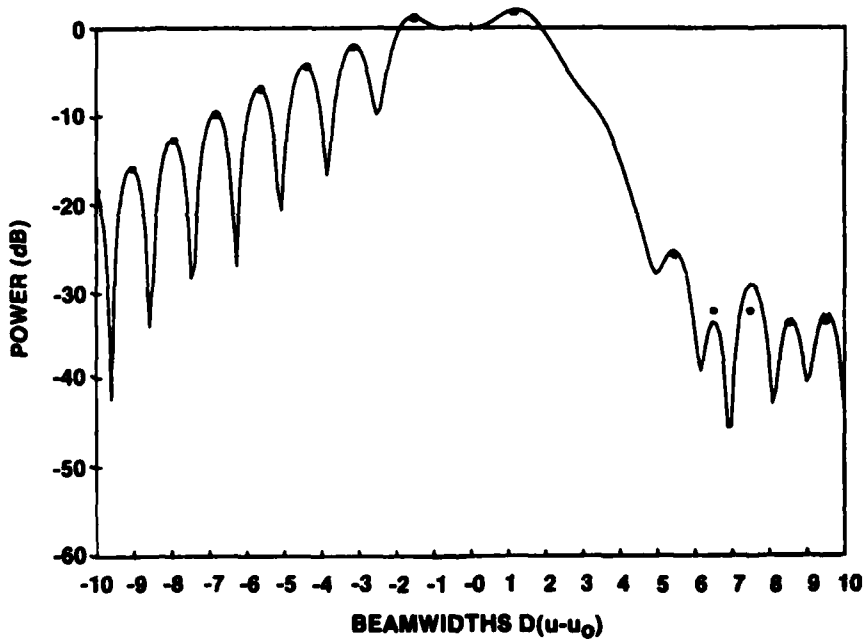

Figure C1. Comparison of Patterns Obtained by Scalar Aperture Field Integration (Solid Line) and by Vector Current Integration (Circles)

To address the second question we compare the diffraction patterns computed by the aperture integration method and Geometrical Theory of Diffraction (GTD), respectively. The latter method is used as a reference, since it correctly describes the far-out sidelobes. Such a comparison is quite illustrative and will be outlined below, since rather surprisingly, we were unable to find it explicitly in the literature.

We consider the 2-D case of a parabolic cylinder, diameter D and focal distance F, illuminated by a focal line source. The geometry and notations are shown in Figure C2. Note that the reflector rim is not necessarily a knife edge, but a general wedge of angle ϕ_w. The feed has a symmetric y-polarized field pattern such that $E(s,\psi) = E(s,-\psi)$. If we trace a ray tube of angular cross-section $d\psi$ from the feed to the aperture we find that it intercepts an aperture element

$$dx = \frac{F}{\cos^2 \psi/2}\, d\psi = s_f\, d\psi \quad , \tag{C1}$$

where s_f is the distance from the focus to the reflection point on the cylinder. Thus, the ray tube has the same cross-section area at the reflector as at the aperture. The incident field $E_i(\psi)$ at the reflector is assumed normalized such that $|E_1|^2$ is the intensity in Watts per meter. Since the power within the ray tube is constant it follows that the normalized aperture distribution

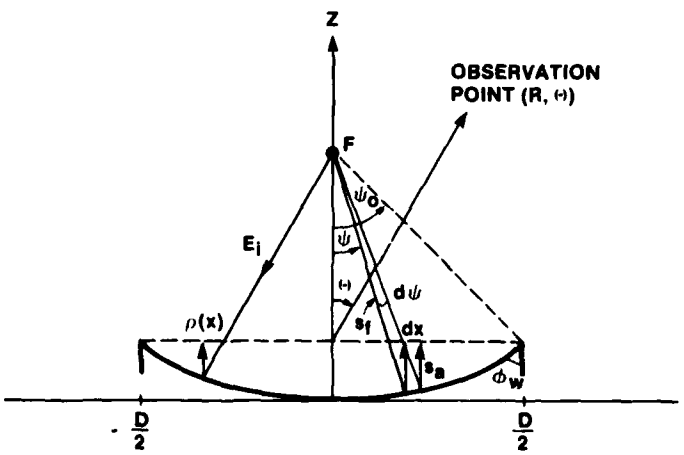

Figure C2. Geometry of Parabolic Reflector with Line Source Feed

$$\rho(x) = E_i(\psi)\, e^{-jks_a} \quad , \tag{C2}$$

where the phase factor expresses the phase delay over the distance s_a from the reflector to the aperture.

The far field based on aperture integration is now obtained as follows. Each aperture element dx represents a source of strength $\rho(x)dx$, which radiates a cylindrical wave, described by the Hankel function $H_o^{(2)}(kr)$. The total far field can be shown to be[C2]

$$E^a = -\frac{k}{2} \int_{-D/2}^{D/2} \rho\, H_o^{(2)}(kr)\, dx$$

$$= -\sqrt{\frac{jk}{2\pi R}}\, e^{-jkR} \int_{-D/2}^{D/2} \rho\, e^{jkx\sin\theta}\, dx \quad , \tag{C3}$$

where the superscript a denotes aperture integration, and we have made the usual far-field approximations for the Hankel function and the distance r from the aperture element dx to the observation point. In the sidelobe region the integral reduces essentially to two end contributions,[C3] so that

$$E^a \simeq -\frac{\sqrt{j\lambda}}{\pi}\, \frac{e^{-jkR}}{\sqrt{R}}\, \rho(D/2)\, \frac{\sin(\frac{1}{2}kD\sin\theta)}{\sin\theta} \quad . \tag{C4}$$

Finally, in view of Eq. (C2) we obtain

$$E^a \simeq -\frac{\sqrt{j\lambda}}{\pi}\, \frac{e^{-jkR}}{\sqrt{R}}\, E_i(\psi_o)\, \frac{\sin(\frac{1}{2}kD\sin\theta)}{\sin\theta} \quad . \tag{C5}$$

The far field E^g according to the GTD method consist of the sum of the fields E_1 and E_2, scattered at the left and right edge of the reflector, as shown in Figure C3. Due to the feed symmetry the incident field is equal at both edges we have in the far zone

---

C2. Harrington, R. (1961) Time-Harmonic Electromagnetic Fields, McGraw Hill, N.Y., p. 288.

C3. Felsen, L., and Marcuvitz, N. (1973) Radiation and Scattering of Waves, Prentice-Hall, N.J., p. 387.

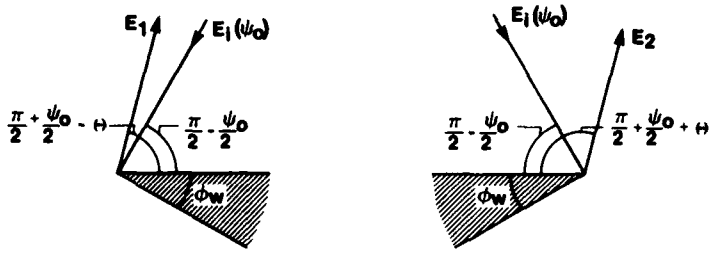

Figure C3. Reflector Edge Geometry for GTD Analysis

$$E^g \simeq D_1\, E_i(\psi_o)\, \frac{e^{-jk(R+\frac{1}{2}D\sin\theta)}}{\sqrt{R}} + D_2\, E_i(\psi_o)\, \frac{e^{-jk(R-\frac{1}{2}D\sin\theta)}}{\sqrt{R}} \quad , \tag{C6}$$

where D_1 and D_2 are edge diffraction coefficients. Setting momentarily

$$u' = \frac{1}{2}\, kD \sin\theta \tag{C7}$$

we obtain from Eq. (C6)

$$E^g \simeq [(D_1 + D_2) \cos u' - j(D_1 - D_2) \sin u']\, E_i(\psi_o)\, \frac{e^{-jkR}}{\sqrt{R}} \quad . \tag{C8}$$

We use Keller's original diffraction coefficients, see, for instance Reference C4. When the incidence and scattering angles appropriate for our geometry (see Figure C3) are substituted in these coefficients, the result is

$$D_1 + D_2 = C\left[\frac{1}{\cos\frac{\pi}{n} - \cos\frac{\psi_o-\theta}{n}} + \frac{1}{\cos\frac{\pi}{n} - \cos\frac{\psi_o+\theta}{n}} - \frac{1}{\cos\frac{\pi}{n} - \cos\frac{\pi-\theta}{n}} - \frac{1}{\cos\frac{\pi}{n} - \cos\frac{\pi+\theta}{n}}\right]$$

$$D_1 - D_2 = C\left[\frac{1}{\cos\frac{\pi}{n} - \cos\frac{\psi_o-\theta}{n}} - \frac{1}{\cos\frac{\pi}{n} - \cos\frac{\psi_o+\theta}{n}} - \frac{1}{\cos\frac{\pi}{n} - \cos\frac{\pi-\theta}{n}} + \frac{1}{\cos\frac{\pi}{n} - \cos\frac{\pi+\theta}{n}}\right] \quad , \tag{C9}$$

C4. Balanis, C.A. (1982) Antenna Theory, Harper & Row, N.Y., p. 509.

where

$$C = e^{-j\pi/4} \sin(\pi/n) / (n\sqrt{2\pi k})$$

$$n = 2 - \phi_w/\pi \quad . \tag{C10}$$

We now investigate the behavior of $D_1 + D_2$ and $D_1 - D_2$ in the sidelobe region near the main beam, where $|\theta| << 1$. In general ψ_o, n and π will be independent parameters and therefore we obtain

$$\lim_{\theta \to 0} (D_1 + D_2) = C \left[\frac{2}{\cos\frac{\pi}{n} - \cos\frac{\psi_o}{n}} + \frac{\cos\frac{\pi}{n}}{\sin^2\frac{\pi}{n}} \right] \quad . \tag{C11}$$

For $D_1 - D_2$ however, the situation is different and there we find

$$D_1 - D_2 \simeq C \frac{2}{\sin\frac{\theta}{n} \sin\frac{\pi}{n}} \quad , \tag{C12}$$

which is unbounded when $\theta \to 0$. Substituting the above expressions into Eq. (C9) yields

$$E^g \simeq \frac{e^{j\pi/4}\sqrt{\lambda}}{\pi n \sin(\theta/n)} E_i(\psi_o) \frac{e^{-jkR}}{\sqrt{R}} [\sin u' + j\epsilon \cos u'] \quad , \tag{C13}$$

where

$$\epsilon = \left[\frac{1}{\cos\frac{\pi}{n} - \cos\frac{\psi_o}{n}} + \frac{\cos\frac{\pi}{n}}{2\sin^2\frac{\pi}{n}} \right] \sin\frac{\pi}{n} \sin\frac{\theta}{n} \quad . \tag{C14}$$

The second term within the bracket in Eq. (C13) is in phase quadrature to the first one and has a much smaller magnitude. Its main effect is to fill in the pattern nulls. For reflector edge angles $w_\phi \leq 90^o$ and normal F/D ratios we find that

$$|\epsilon(\theta, \psi_o, n)| \leq |\sin\frac{\theta}{n}| \quad . \tag{C15}$$

The second term may therefore be neglected and as long as

$$|\theta| \leq \theta_{max} = \frac{1}{4} \quad , \tag{C16}$$

the relative error in the field pattern envelope will be less than 1/32, or about 3 percent. Thus, we finally obtain

$$E^g \simeq \frac{\sqrt{j\lambda}}{\pi n \sin(\theta/n)} \frac{e^{-jkR}}{\sqrt{R}} E_i(\psi_o) \sin(\tfrac{1}{2}kD \sin\theta) \quad . \tag{C17}$$

Comparing E^g above with E^a of Eq. (C5), we find that the ratio

$$\frac{E^a}{E^g} = \frac{n \sin(\theta/n)}{\sin\theta} \simeq 1 + \frac{\theta^2}{6}\left(1 - \frac{1}{n^2}\right) \leq 1 + \frac{\theta^2_{max}}{6} = 1 + \frac{1}{96} \quad , \tag{C18}$$

where we have substituted Eq. (C16) for θ_{max}. The relative difference between E^a and E^g thus is 1/96, or about 1 percent. This error adds to the 3 percent relative error in E^a incurred earlier.

In summary, we have shown that the sidelobe pattern, in particular the pattern envelope and the sidelobe positions, is accurately determined by the aperture integration method out to angles of $\pm 15^o$ or $\pm 1/4$ (D/λ) beamwidths around the main beam. In this sector the sidelobes can be viewed to be determined by the aperture field alone, independent of the reflector edge geometry. Consequently, even when we scan the main beam by imposing a linear phase taper over the aperture, we can expect aperture integration to accurately predict the sidelobe pattern over a $\pm 1/4(D/\lambda)$ beamwidths sector, but this time centered around the scan direction.

The above conclusions are independent of the feed polarization, as can be easily shown. Also they apply equally well for a circular reflector as for the cylindrical reflector considered here, since the diffraction coefficients are identical in the two cases. However, we feel that the idealized geometry considered here may be a particularly favorable case and that caution should be exercised when applying these conclusions to more general problems, as for example, offset reflectors, highly tapered illuminations, or illuminations with large amplitude and phase errors.

MISSION
of
Rome Air Development Center

RADC plans and executes research, development, test and selected acquisition programs in support of Command, Control Communications and Intelligence (C^3I) activities. Technical and engineering support within areas of technical competence is provided to ESD Program Offices (POs) and other ESD elements. The principal technical mission areas are communications, electromagnetic guidance and control, surveillance of ground and aerospace objects, intelligence data collection and handling, information system technology, ionospheric propagation, solid state sciences, microwave physics and electronic reliability, maintainability and compatibility.

Printed by
United States Air Force
Hanscom AFB, Mass. 01731